

# Origin of Moiré Potentials in $\text{WS}_2/\text{WSe}_2$ Heterobilayers: Contributions from Lattice Reconstruction and Interlayer Charge Transfer

Youwen Wang,<sup>1</sup> Nanya Gao,<sup>1</sup> and Qingjun Tong<sup>1,\*</sup>

<sup>1</sup>*School of Physics and Electronics, Hunan University, Changsha 410082, China*

Moiré superlattices formed in  $\text{WS}_2/\text{WSe}_2$  heterobilayers have emerged as an exciting platform to explore the quantum many-body physics. The key mechanism is the introduction of moiré potentials for the band-edge carriers induced by the lateral modulation of interlayer interactions. This trapping potential results in the formation of flat bands, which enhances the strong correlation effect. However, a full understanding of the origin of this intriguing potential remains elusive. In this paper, we present a comprehensive investigation of the origin of moiré potentials in both R-type and H-type moiré patterns formed in  $\text{WS}_2/\text{WSe}_2$  heterobilayers. We show that both lattice reconstruction and interlayer charge transfer contribute significantly to the formation of moiré potentials. In particular, the lattice reconstruction induces a nonuniform local strain, which creates an energy modulation of  $\sim 200$  meV for the conduction band-edge state located at  $\text{WS}_2$  layer and  $\sim 20$  meV for the valence band-edge state located at  $\text{WSe}_2$  layer. In addition, the lattice reconstruction also introduces a piezopotential energy, whose amplitude ranges from  $\sim 40$  to  $\sim 90$  meV depending on the stacking and band-edge carrier. The interlayer charge transfer induces a built-in electric field, resulting in an energy modulation of  $\sim 80$  meV for an R-type moiré and  $\sim 40$  meV for an H-type moiré. Taking into account both effects from lattice reconstruction and interlayer charge transfer, the formation of moiré potential is well understood for both R-type and H-type moirés. This trapping potential localizes the wavefunctions of conduction and valence bands around the same moiré site for an R-type moiré, while around different moiré site for an H-type one. Our work not only provides an efficient method to study lattice-mismatch induced moiré patterns, but also gives help in understanding the intriguing moiré physics in  $\text{WS}_2/\text{WSe}_2$  heterobilayers.

## I. INTRODUCTION

van der Waals (vdW) heterostructures provide a powerful approach to engineer novel physics and functional devices [1–3]. A characteristic feature of vdW heterostructures is the presence of a moiré pattern because of the lattice mismatch and/or twisting [4]. This moiré superlattice formed in magic-angle twisted bilayer graphene has led to the experimental discovery of superconducting and correlated insulating states [5, 6]. Another frontier of recent studies is the moiré superlattice formed in transition metal dichalcogenides (TMDs), which have many advantageous optoelectronic properties [7–10]. Because of the strong Coulomb interaction, moiré patterns formed in  $\text{WS}_2/\text{WSe}_2$  heterobilayers are of particular interest, which have emerged as a rich playground for exploration of novel excitonic and electronic states, such as moiré excitons [11–15], Mott and generalized Wigner crystal states [16–28]. The lattice mismatch between  $\text{WS}_2$  and  $\text{WSe}_2$  is about 4%, which gives a moiré pattern of  $\sim 8$  nm [29–31]. The electronic structure of a  $\text{WS}_2/\text{WSe}_2$  heterobilayer is of type-II band alignment, where the conduction and valence bands are located at  $\text{WS}_2$  and  $\text{WSe}_2$  layer respectively, and the excitonic ground state is of an interlayer configuration [32–34]. Because of the breaking of inversion symmetry in the monolayer TMDs, the formed moiré pattern has two types, named as R-type and H-type respectively [35]. Furthermore, recent experimental studies have shown that both in-plane and

out-of-plane lattice reconstructions in  $\text{WS}_2/\text{WSe}_2$  heterobilayers are remarkable, which are believed to impact greatly their optical and electronic properties [30, 31].

The key to the emergence of novel physics in moiré superlattices lies in the formation of moiré potential, which results in nearly flat minibands with localized electronic and excitonic states [36, 37]. In a long-period moiré pattern, the interlayer atomic configuration locally resembles lattice commensurate structures while changes smoothly over long range [35, 38]. Because the interlayer interaction generally depends on the stacking order, such a spatial change of interlayer configurations then introduces a spatial modulation of interlayer interaction in the moiré pattern [39–44]. This lateral modulation of interlayer interactions then defines a trapping potential (dubbed moiré potential) for the band-edge electronic and excitonic states. It is believed that there are multiple factors that would contribute to the moiré potential. In particular, interlayer hybridization would couple the two layers, which results in a renormalization of their band structures [37, 45]. Furthermore, the lattice reconstruction within each layer induces a local strain, which would change the band structure of each monolayer [46, 47]. In twisted homobilayers or chalcogen-matched heterobilayers, it has been shown that the lattice reconstruction would also introduce a piezoelectric effect that strongly confines band-edge carriers [48–51]. Finally, the interlayer charge transfer induces a built-in electric field, which would shift relatively the band structures of the two layers [52]. However, a comprehensive understanding that takes into account all of these effects and accounts for different moiré types is still lacking.

\* [tongqj@hnu.edu.cn](mailto:tongqj@hnu.edu.cn)

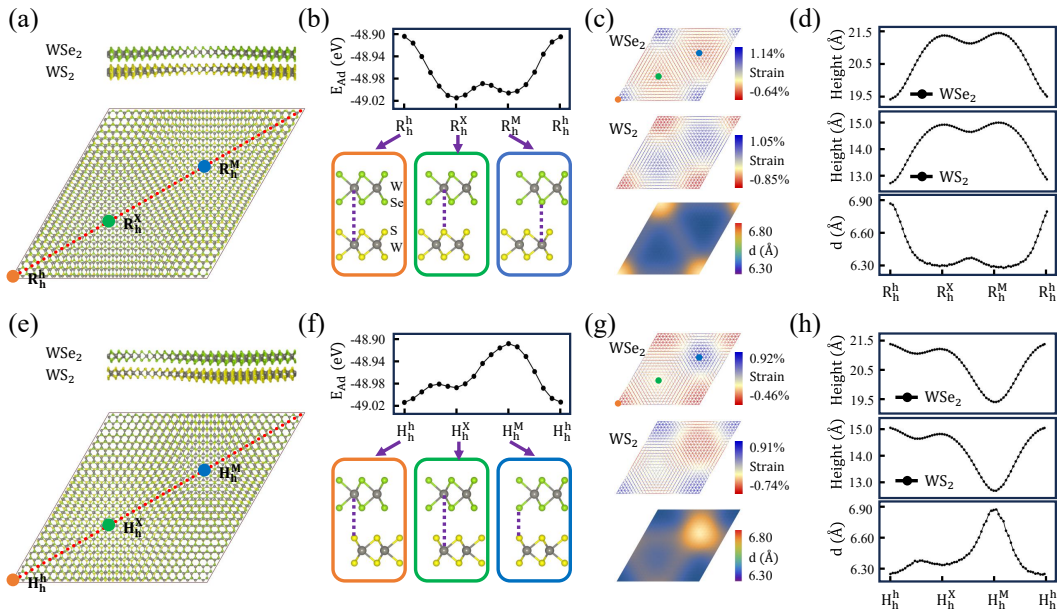


FIG. 1. (a) Relaxed atomic structure of an R-type moiré pattern formed in WS<sub>2</sub>/WSe<sub>2</sub> heterobilayers. The top panel is a lateral view showing strong out-of-plane corrugation. The three high-symmetry locales along the long-diagonal of a moiré unit cell are labeled as  $R_h^h$ ,  $R_h^X$ , and  $R_h^M$ . The moiré periodicity is 8.25 nm formed by a lattice mismatch of 4% between WS<sub>2</sub> and WSe<sub>2</sub> with no relative rotation. (b) Adhesion energy as a function of interlayer stacking along the long diagonal of the relaxed moiré pattern in (a). The interlayer atomic configurations at three high-symmetry locales are given in the lower panel. (c) The extracted lattice-reconstruction induced in-plane strain distribution in the WSe<sub>2</sub> layer (upper) and WS<sub>2</sub> layer (middle). The interlayer distance  $d$  is given in the lower panel, which is defined by the distance between the two W atomic planes. (d) Out-of-plane corrugation of WSe<sub>2</sub> layer (upper) and WS<sub>2</sub> layer (middle) and the interlayer distance (lower) along the long diagonal of the relaxed moiré pattern. (e)-(h) The same as (a)-(d) for the an H-type moiré pattern, where the upper WSe<sub>2</sub> layer has a rotation of 180 degree relative to the lower WS<sub>2</sub> layer.

In this work, we present a comprehensive study on the origin of moiré potentials in both R-type and H-type moiré patterns formed in WS<sub>2</sub>/WSe<sub>2</sub> heterobilayers. We find that both types of moiré show strong lattice reconstruction in both in-plane and out-of-plane directions. From the calculation of the miniband structures, we show that in the R-type moiré, the conduction and valence band-edge states are trapped around the same moiré site. While in the H-type moiré, they are trapped around different moiré sites. This different localization behavior dates back to the distinct morphology of moiré potentials of the two types of moiré, which is contributed by lattice-reconstruction induced local strain and interlayer charge transfer. In particular, we find that, for both R-type and H-type moirés, the lattice-reconstruction induced local strain results in a strong energy modulation with an amplitude of  $\sim 200$  meV for the conduction band-edge states, while it is of nearly an order smaller for the valence band-edge states. In addition, the lattice reconstruction also introduces a piezopotential energy, whose amplitude ranges from  $\sim 40$  to  $\sim 90$  meV depending on the stacking and band-edge carrier. We also find significant interlayer charge transfer effect in both types of moiré, which leads to band modulations with an amplitude of  $\sim 80$  meV for the R-type moiré and  $\sim 40$  meV

for the H-type moiré. Taking into account the effects from local-strain induced band modulation, piezopotential energy and interlayer charge transfer, the localization behavior of band-edge states in both R-type and H-type moirés can be properly explained.

The rest of the paper is organized as follows. In Sec. II, we give the atomic structures of the moiré patterns in both R-type and H-type WS<sub>2</sub>/WSe<sub>2</sub> heterobilayers and illustrate their detailed lattice reconstruction effect in both in-plane and out-of-plane directions. The miniband structures of the moiré patterns are given in Sec. III. The wavefunctions of the conduction and valence bands and their localization behaviors are also presented. In Sec. IV, we discuss the origin of moiré potentials for both types of moiré patterns, and explain the localization behavior of band-edge states. Finally, discussions on the relevance of our moiré potential to recent experiments and a summary are given in Sec. V. The details of first-principles calculations are given in the Appendix.

## II. ATOMIC STRUCTURES OF MOIRÉ PATTERNS IN WS<sub>2</sub>/WSE<sub>2</sub> HETEROBILAYERS

In their monolayer forms, TMDs break the inversion symmetry and possess threefold rotation symmetry with the rotation center located at a hexagon center (h), chalcogen (X) site, and metal (M) site respectively [29]. As a result, when stacking together, TMD heterobilayers may have two types of moiré patterns, i.e. with lattice mismatch and/or rotation angle near 0° (R-type) or 60° (H-type), as shown in Figs. 1(a) and 1(e). In a long-period moiré, the interlayer atomic configuration changes smoothly, which can be characterized by a vector  $\mathbf{r}$  that defined in a unit cell of the monolayer [35]. In our study of WS<sub>2</sub>/WSe<sub>2</sub> heterobilayers, there exist three moiré sites with threefold rotation symmetry in both types of moirés. We name these moiré sites as  $R_h^\mu$  and  $H_h^\mu$  in R-type and H-type stacking respectively, where the  $\mu$  site of the WSe<sub>2</sub> layer vertically aligned with the  $h$  site of the WS<sub>2</sub> layer.

Because of distinct interlayer stacking registry, the locally commensurate heterobilayers in the moiré have different adhesion energies. First-principles calculations given in Figs. 1(b) and 1(f) show that, for R-type WS<sub>2</sub>/WSe<sub>2</sub> moiré, the  $R_h^X$  stacking is the lowest energy configuration (with largest adhesion energy), while  $R_h^h$  is the highest one. For H-type moiré, the  $H_h^h$  stacking is the lowest energy configuration, while  $H_h^M$  is the highest one. Because of this stacking dependent adhesion energy, the moiré lattice experiences strong structure reconstruction to reduce total energy. The final relaxed structure is then determined by the competition between the intralayer elastic energy caused by lattice reconstruction and the interlayer adhesion energy [48–51, 53, 54]. We use LAMMPS to perform the structural relaxation with the calculation details given in Appendix. For R-type moiré, TMD lattice would relax itself to enlarge the  $R_h^X$  stacking area and reduce the  $R_h^h$  stacking area [Fig. 1(a)]. For H-type moiré, TMD lattice would relax itself to enlarge the  $H_h^h$  stacking area and reduce the  $H_h^M$  stacking area [Fig. 1(e)]. We note that, because of this lattice reconstruction, the mapping between the local registry  $\mathbf{r}$  and moiré location  $\mathbf{R}$  becomes nonlinear.

As a result of this structure reconstruction, the moiré lattices feature both in-plane and out-of-plane deformations in each constituent monolayer. Figures 1(c) and 1(g) show the extracted lattice-reconstruction-induced local strain in each layer. The magnitude of this local strain can reach  $\sim 1\%$  for both R-type and H-type moirés. In particular, for R-type case, the local strain is compressive at  $R_h^X$  and  $R_h^M$  stackings and tensile at  $R_h^h$  stacking on the WSe<sub>2</sub> layer. While on the WS<sub>2</sub> layer, the local strain is opposite. For H-type case, the local strain is compressive at  $H_h^h$  stacking and tensile at  $H_h^M$  site on the WSe<sub>2</sub> layer. While on the WS<sub>2</sub> layer, the local strain is opposite. In addition, there exists a strong out-of-plane lattice reconstruction as shown in Figs. 1(d) and 1(h). In particular, for both types of moirés, there is a modula-

tion of interlayer distance. The largest distance is at  $R_h^h$  stacking for R-type and  $H_h^M$  stacking for H-type, both of which have chalcogen atoms sitting directly to each other. More interestingly, we find a strong out-of-plane modulation in each monolayer, both of which in the two types of moirés can reach as high as 2 Å, which is almost one third of the interlayer distance.

## III. FLAT MINIBAND AND THE LOCALIZATION OF BAND-EDGE STATES

We now turn to studying the electronic structures of the moiré patterns formed in WS<sub>2</sub>/WSe<sub>2</sub> heterobilayers, with the focus on the flat bands formed near the band edges and their localization behavior. The calculation details are given in Appendix. Figure 2(a) shows the first-principles calculated miniband structure of an R-type moiré pattern, with the orbital projections indicated explicitly. A series of nearly flat bands are observed in both conduction and valence bands. Compared with the bandwidths in valence bands, the ones in conduction bands are much smaller, suggesting a more compact trapping effect therein. From the analysis of the orbital components, we find that the conduction band-edge states are mainly composed of  $d_{z^2}$  orbital, and the valence band-edge states are mainly composed of  $d_{x^2-y^2}$  and  $d_{xy}$  orbitals. This suggests that the conduction miniband originates from the conduction band at K point of WS<sub>2</sub> layer and the valence miniband originates from the valence band at K point of WSe<sub>2</sub> layer [29]. The distribution of the wavefunctions at the band edges in the moiré unit cells is given in Figs. 2(b) and 2(c). From the lateral view, we find that the conduction band-edge state is localized at the WS<sub>2</sub> layer, while the valence band-edge state is localized at the WSe<sub>2</sub> layer confirming the type-II band alignment. The top views show that both the conduction and valence band-edge states are localized around  $R_h^M$  site. The former is more localized than the latter, because its miniband is flatter.

Figure 3(a) shows the band structure of an H-type moiré pattern, which features flat bands in both conduction and valence minibands similar to the R-type case. The orbital projection suggests that these flat bands also originate from the band-edge states from K point of the WS<sub>2</sub> and WSe<sub>2</sub> layer respectively. However, different from the R-type moiré, the wavefunctions of the conduction and valence band-edge states are located around different moiré sites. In particular, the conduction band-edge state is localized around  $H_h^h$  site [Fig. 3(b)], while the valence band-edge one is localized around  $H_h^X$  site [Fig. 3(c)]. This vertical misalignment of electron and hole wavefunctions is responsible for the experimental observation of intercell moiré exciton complexes with large in-plane electrical quadrupole moments [28].

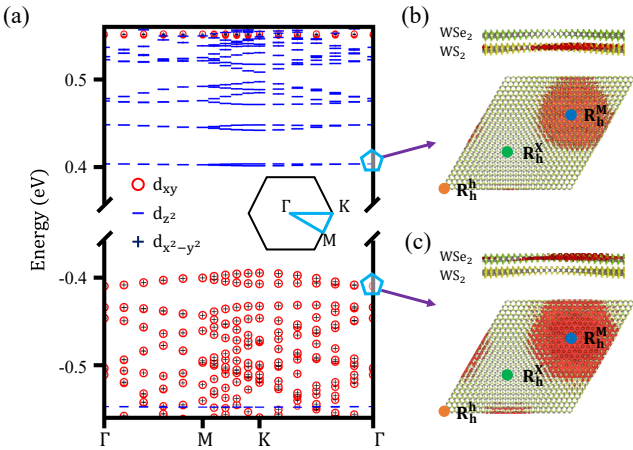


FIG. 2. (a) Electronic band structure of a relaxed R-type  $WS_2/WSe_2$  moiré pattern along the high-symmetry lines in the hexagonal mini-Brillouin zone (inset). The projected orbital contributions are indicated. The distribution of the wavefunctions in the moiré unit cell for the conduction (b) and valence (c) band-edge states at the energy points marked by the pentagons in (a), both of which are localized around  $R_h^M$  site. The top panels show the lateral views.

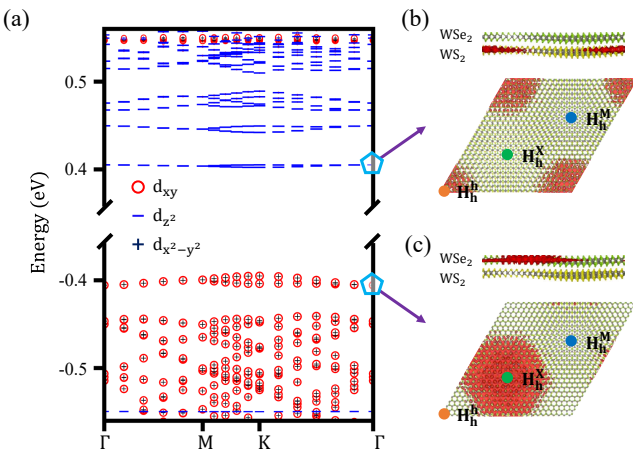


FIG. 3. (a) Electronic miniband structure of a relaxed H-type  $WS_2/WSe_2$  moiré pattern along the high-symmetry lines in the hexagonal mini-Brillouin zone. The projected orbital contributions are indicated. The distribution of the wavefunctions in the moiré unit cell for the conduction (b) and valence (c) band-edge states at the energy points marked by the pentagons in (a), which are localized around  $H_h^h$  site and  $H_h^X$  site respectively. The top panels show the lateral views.

#### IV. ORIGIN OF MOIRÉ POTENTIALS

The distinct localization behavior of band-edge states in the two types of moiré patterns suggests that they have different moiré potential profiles contributed by various factors. Because of the large band offset ( $\sim 860$  meV for the conduction band and  $\sim 630$  meV for the valence band), the interlayer hybridization is significantly

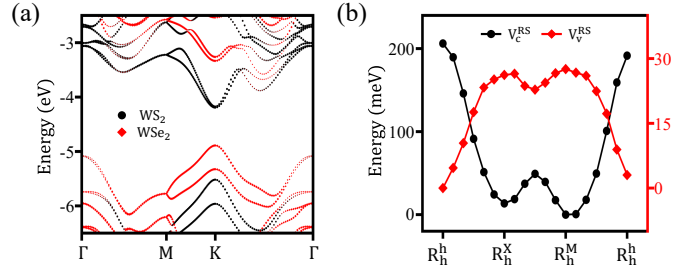


FIG. 4. (a) Layer-projected band structure of a  $WS_2/WSe_2$  heterobilayer. The type-II band edges are located at K point. A commensurate  $R_h^X$  stacking is adopted. (b) Modulation of conduction band-edge energy of monolayer  $WS_2$  ( $V_c^{RS}$  as black line with dots) and valence band-edge energy of monolayer  $WSe_2$  ( $V_v^{RS}$  as red line with diamonds) as a function of local strain adopted along the long diagonal of Fig. 1(c).

quenched in the  $WS_2/WSe_2$  heterobilayer [cf. the layer-projected band structure in Fig. 4(a)]. We then focus on studying the effects from lattice reconstruction and interlayer charge transfer in the following. We note that the lattice reconstruction mainly affects the constituent monolayers, so it is sufficient to study the effect of lattice-reconstruction-induced local strain by using TMD monolayers. In particular, based on the layer projection shown in Fig. 4(a), we find that it is sufficient to study the local strain effect on the conduction band of monolayer  $WS_2$  and valence band of monolayer  $WSe_2$  at K point. This adoption of TMD monolayers can avoid the introduction of additional strain ( $\sim \pm 2\%$ ) to construct commensurate bilayers and also distinguish the contribution of local strain from interlayer charge transfer that happens in a bilayer. In the following, we discuss the R-type and H-type moirés separately.

#### A. R-type moiré

Figure 4(b) shows the energy modulations of conduction band of monolayer  $WS_2$  ( $V_c^{RS}$  as black line with dots) and valence band of monolayer  $WSe_2$  ( $V_v^{RS}$  as red line with diamonds) as a function of local strain extracted from the relaxed R-type moiré pattern as shown in Fig. 1(c). We find that this strain induced band modulation in the conduction band is almost an order larger than that in the valence band, which is consistent with previous calculations [55]. In the following, we first focus on the energy profile of the conduction band of monolayer  $WS_2$ . The magnitude of this modulation reaches as high as  $\sim 200$  meV, as has been experimentally observed by recent STM study [56]. More importantly, the local minima of this energy profile are located at  $R_h^X$  and  $R_h^M$  stackings with a small energy difference of 13 meV, which suggests that the electrons should be localized around these two stackings. However, our calculation of wavefunction in Fig. 2(b) shows that electrons are only localized around  $R_h^M$  stacking. We note that the flat miniband

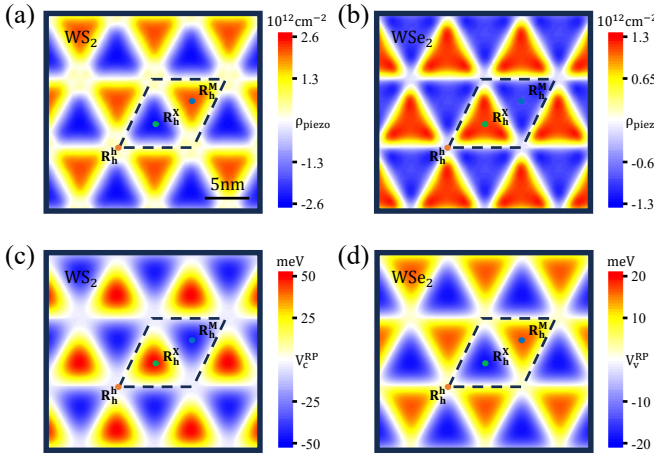


FIG. 5. (a)(b) Lattice-reconstruction-induced piezochARGE densities  $\rho_{\text{piezo}}$  in the (a)  $\text{WS}_2$  and (b)  $\text{WSe}_2$  layer respectively. (c), (d) Piezopotential energy induced by piezoelectric charge shown in (a) and (b) with the screening effect considered.

above lowest conduction one is still localized around  $R_h^M$  stacking, which is attributed to the spin splitting of conduction band in monolayer  $\text{WS}_2$  with an energy separation of  $\sim 30$  meV [29]. Therefore additional contributions are needed to explain the localization behavior of these miniband-edge states.

Because of inversion symmetry breaking in monolayer TMDs, the inhomogeneous strain induced by lattice reconstruction can result in a piezoelectric effect [48–51]. The piezochARGE density is given by

$$\rho_{\text{piezo}}^{(\ell)}(\mathbf{r}) = e_{11}^{(\ell)} \left[ 2 \partial_x u_{xy}^{(\ell)} + \partial_y (u_{xx}^{(\ell)} - u_{yy}^{(\ell)}) \right], \quad (1)$$

where  $\ell = \{t, b\}$  is the layer index and  $|e_{11}| = \{2.03 \times 10^{-10} \text{ C/m for } \text{WSe}_2, 2.74 \times 10^{-10} \text{ C/m for } \text{WS}_2\}$  is the piezoparameter [57]. The strain tensor is defined as the spatial gradients of the displacement field, i.e.  $u_{ij} = \frac{1}{2}(\partial_i u_j + \partial_j u_i)$ . The spatial distributions of  $\rho_{\text{piezo}}$  in the two layers are given in Figs. 5(a) and 5(b). This piezochARGE density further induces a screening one  $\rho_{\text{ind}}^{(\ell)} = \alpha_{2\text{D}}^{(\ell)} \nabla_{\mathbf{r}}^2 \phi_{\text{piezo}}^{(\ell)}$ , where  $\phi_{\text{piezo}}^{(\ell)}$  is the electric potential produced by the piezochARGEs. The in-plane 2D polarizability of the two monolayer is related to the static in-plane dielectric permittivity  $\epsilon_{\parallel} = \{15.9 \text{ for } \text{WSe}_2, 14.4 \text{ for } \text{WS}_2\}$  and interlayer distance  $d_0 = 6.3 \text{ \AA}$  as,  $\alpha_{2\text{D}}^{(\ell)} = d_0(\epsilon_{\parallel} - 1)/4\pi$  [58]. The total potential  $\phi^{(\ell)}$  is then obtained by solving the Poisson equation. Figures 5(c) and 5(d) show the distribution of potential energy  $V_{(\ell)}^{RP} = -e\phi^{(\ell)}$  induced by this piezoelectric effect. We find that the magnitude of this potential reaches as high as  $\sim 90$  meV in the  $\text{WS}_2$  layer with the minimum located at  $R_h^M$  stacking, while it is  $\sim 40$  meV in the  $\text{WSe}_2$  layer with the maximum located at  $R_h^M$  stacking as well.

Generally, for a vdW layered material, there exists a finite interlayer charge transfer between the constituent

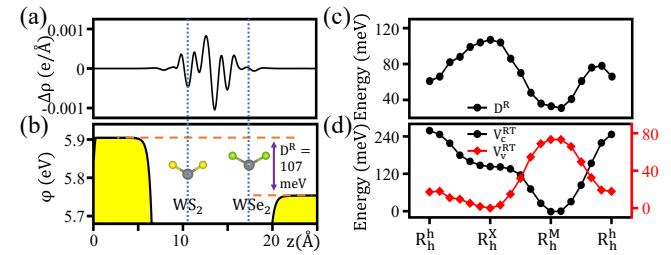


FIG. 6. (a) Plane-averaged charge density difference  $\Delta\rho$  for a commensurate  $R_h^X$  stacking. (b) Electrostatic potential  $\varphi$  obtained from the first-principles calculations including the contributions from the ionic and Hartree potentials. The charge redistribution results in a vacuum level difference  $D^R$  between the two layers. (c)  $D^R$  as a function of stacking orders adopted along the long-diagonal of an R-type moiré in Fig. 1(a). (d) The total moiré potential  $V_{c/v}^{RT}$  for the conduction band (black line with dots) and valence band (red line with diamonds) contributed by local strain and interlayer charge transfer.

layers, which is responsible for the sliding ferroelectricity [59]. It has been shown that this charge transfer depends on the interlayer stacking, which can contribute to the moiré potentials [52]. Figure 6(a) shows the first-principles calculated plane-averaged charge density difference, which suggests that there is a finite interlayer charge transfer across the  $\text{WS}_2/\text{WSe}_2$  heterointerface. This charge redistribution results in a built-in electric field, which leads to a vacuum level difference  $D^R$  across the two layers as indicated in Fig. 6(b). This potential difference agrees well with the one obtained by solving directly the Poisson equation, which suggests that the main effect of interlayer charge transfer is the introduction of a Stack effect that shifts relatively the band structures of the two layers [52]. In particular, the induced electric potentials are  $V_c^{RC} = D^R/2$  for the  $\text{WS}_2$  layer and  $V_v^{RC} = -D^R/2$  for the  $\text{WSe}_2$  layer. Importantly, this interlayer charge transfer depends on the stacking order, which further results in a stacking dependence of the built-in electric field and hence the Stack-shift energy. Figure 6(c) shows the vacuum level difference  $D^R$  as a function of different stackings along the long diagonal of the lattice-relaxed moiré pattern, from which an energy modulation on the order of 80 meV is observed. In particular, with a smaller atomic shell number, the S atom is easier to attract electrons from the W atom than the Se atom. As a result, for  $R_h^X$  configuration, in which the S atom of  $\text{WS}_2$  is vertically aligned with W atom of  $\text{WSe}_2$ , the charge transfer is largest. On the other hand, for  $R_h^M$  configuration, the charge transfer is smallest. For  $R_h^h$  configuration, the large interlayer distance also suppresses the interlayer charge transfer. Accordingly, this potential profile shows local minimum and maximum at  $R_h^M$  and  $R_h^X$  site respectively. Finally, taking into account the effects from local-strain-induced band modulation, piezopotential energy and interlayer charge transfer, the total energy profile of the conduction band [ $V_c^{RT} \equiv V_{c/v}^{RS} + V_{c/v}^{RP} + V_c^{RC}$  as black line with

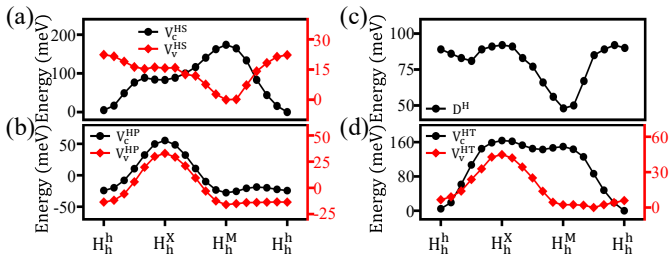


FIG. 7. (a) Modulation of conduction band-edge energy of monolayer WS<sub>2</sub> ( $V_c^{HS}$  as black line with dots) and valence band-edge energy of monolayer WSe<sub>2</sub> ( $V_v^{HS}$  as red line with diamonds) as a function of local strain adopted along the long-diagonal of Fig. 1(g). (b) The piezopotential energy induced by piezoelectric charge with the screening effect considered in the WS<sub>2</sub> ( $V_c^{HP}$  as black line with dots) and WSe<sub>2</sub> layer ( $V_v^{HP}$  as red line with diamonds). (c) The vacuum level difference  $D^H$  across the heterointerfaces with stacking orders adopted along the long-diagonal of an H-type moiré in Fig. 1(e). (d) The total moiré potential  $V_{c/v}^{HT}$  for the conduction band (black line with dots) and valence band (red line with diamonds) contributed by local strain and interlayer charge transfer.

dots in Fig. 6(d)] gives a strong trapping at  $R_h^M$  site. This well explains the localization behavior of conduction miniband-edge state shown in Fig. 2(b).

The above discussion of moiré potential for conduction miniband-edge state also holds for the valence miniband-edge one, which is located at WSe<sub>2</sub> layer. The red line with diamonds in Fig. 6(d) shows the stacking dependence of the total hole potential ( $V_v^{RT} \equiv V_v^{RS} + V_v^{RP} + V_v^{RC}$ ) contributed from the local-strain-induced band modulation, piezopotential energy and interlayer charge transfer. We note that because of the opposite effective mass, valence band states (holes) are trapped at the local maximum of the moiré potential. The calculated total potential profile shows a local maximum at  $R_h^M$  site, which well explains the localization behavior of valence miniband-edge state as shown in Fig. 2(c). Because the overall potential profile of  $V_v^{RT}$  is much smoother than that of  $V_c^{RT}$ , the topmost valence miniband is relatively dispersive and, accordingly, the distribution of the wavefunction is more extended than that of conduction miniband.

### B. H-type moiré

We now turn to studying the H-type moiré, with the focus on joint contributions from lattice-reconstruction induced local strain and interlayer charge transfer. For the conduction band, based on the local strains in WS<sub>2</sub> layer extracted from the relaxed H-type moiré pattern as shown in Fig. 1(g), we find a strong modulation with a magnitude of 173 meV [ $V_c^{HS}$  as black line with dots in Fig. 7(a)]. This potential profile features a local minimum located at  $H_h^h$  site. In addition, this lattice reconstruction induces a piezopotential energy with a magni-

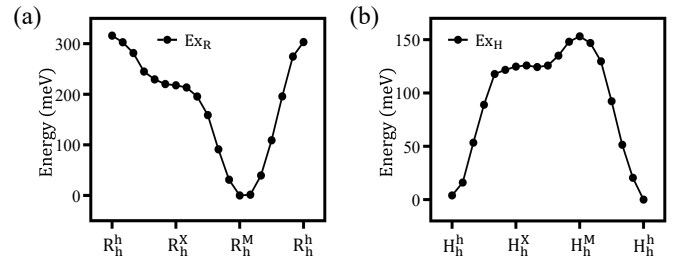


FIG. 8. Excitonic moiré potential along the long-diagonal of an R-type (a) and H-type (b) moiré pattern shown in Fig. 1.

tude of 83 meV [ $V_c^{HP}$  as black line with dots in Fig. 7(b)], which features local minima located at  $H_h^M$  and  $H_h^h$  site. As in the case of R-type moiré, the interlayer charge transfer also induces a stacking dependent energy shift  $V_c^{HC} = D^H/2$  for the WS<sub>2</sub> layer. In particular, Fig. 7(c) shows the first-principles calculated vacuum level difference  $D^H$  across the heterobilayer, whose modulation is nearly half of that of R-type one. It is large at  $H_h^X$  and  $H_h^h$  sites with smaller interlayer distance and smallest at  $H_h^M$  site with largest interlayer distance. The total moiré potential contributed by both local strain and interlayer charge transfer ( $V_{c/v}^{HT} \equiv V_{c/v}^{HS} + V_{c/v}^{HP} + V_{c/v}^{HC}$ ) is given by the black line with dots in Fig. 7(d), in which the minimum is located at  $H_h^h$  site. This is responsible for the localization of wavefunction of conduction miniband as shown in Fig. 3(b).

For the valence band, the band modulation  $V_v^{HS}$  induced by the local strain in the WSe<sub>2</sub> layer extracted from the relaxed H-type moiré pattern in Fig. 1(g) is relatively small with an amplitude of 22 meV, as shown by the red line with diamonds in Fig. 7(a). We note that this potential nearly cancels with the one from interlayer charge transfer  $V_v^{HC} = -D^H/2$  [cf. Fig. 7(c)]. The total potential ( $V_{c/v}^{HT} \equiv V_{c/v}^{HS} + V_{c/v}^{HP} + V_{c/v}^{HC}$ ) is then dominant by the piezopotential energy [red line with diamonds in Figs. 7(b) and 7(d)], which features a magnitude of  $\sim 50$  meV and local maximum at  $H_h^X$  site. This is consistent with the localization behavior of the valence miniband-edge state shown in Fig. 3(c), which is indeed localized around  $H_h^X$  site.

## V. DISCUSSIONS AND CONCLUSIONS

Our results show that the moiré potential is deeper for electrons than that of holes, which generates flatter minibands for the former [cf. Figs. 2(a) and 3(a)]. This agrees with typical doping-dependent photoluminescence experiments on WS<sub>2</sub>/WSe<sub>2</sub> heterobilayer, where the correlation effect is more evident for electron doping than that for hole doping [15, 24, 27, 28]. Furthermore, because the exciton energy is proportional to the difference between electron and hole energy [37], one can define the excitonic moiré potential as  $Ex \equiv V_c^T - V_v^T$ . Figures 8(a) and 8(b) show the excitonic moiré potentials

for both R-type and H-type moirés, which feature double local minima functioning as moiré orbital degree of freedom [12–15]. Recent polarization-resolved photoluminescence studies on H-type WS<sub>2</sub>/WSe<sub>2</sub> heterobilayers have evidenced the moiré-orbital excitons localized at  $H_h^h$  and  $H_h^X$  stackings [15], in good agreement with our calculation shown in Fig. 8(b).

In summary, we have studied the origin of moiré potentials in both R-type and H-type moiré patterns in WS<sub>2</sub>/WSe<sub>2</sub> heterobilayers. We show that both lattice-reconstruction induced local strain and interlayer charge transfer are needed to fully explain the localization behavior of band-edge states. In particular, the local strain results in a modulation of  $\sim 200$  meV at conduction band, while  $\sim 20$  meV at valence band. Furthermore, the lattice reconstruction also introduces a piezopotential energy, whose amplitude ranges from  $\sim 40$  to  $\sim 90$  meV depending on the stacking and band-edge carrier. The interlayer charge transfer across the heterointerface also results in a modulation of band-edge state, with an amplitude of  $\sim 80$  meV for the R-type moiré and  $\sim 40$  meV for the H-type moiré. These contributions together well explain the localization behaviors of band-edge states for both R-type and H-type moirés.

## ACKNOWLEDGMENTS

This work was supported by the National Key Research and Development Program of Ministry of Science and Technology (2022YFA1204700, 2021YFA1200503), the National Natural Science Foundation of China (12374178), and the Fundamental Research Funds for the Central Universities from China.

## APPENDIX: THE FIRST-PRINCIPLES CALCULATIONS

The WS<sub>2</sub>/WSe<sub>2</sub> moiré superlattices contain 3903 atoms and were constructed by 26×26 unit cells of WS<sub>2</sub> and 25×25 unit cells of WSe<sub>2</sub>, whose monolayer lattice constants are 3.17 Å and 3.3 Å, respectively. Struc-

tural relaxation was performed using the LAMMPS [60] package, with intralayer and interlayer interactions described by the Stillinger-Weber [61, 62] potential and Kolmogorov-Crespi [63, 64] potential respectively. Atomic positions were optimized via the conjugate gradient method until the maximum atomic force was below 10<sup>-8</sup> eV/Å. Electronic structure calculations on monolayers and commensurate bilayers were based on density functional theory (DFT) [65]. For the reconstructed moiré superlattice, we employed the SIESTA [66] package using a double- $\zeta$  plus polarization (DZP) basis set with a wavefunction cutoff energy of 100 Ry. The Brillouin zone was sampled only at the  $\Gamma$  point for self-consistent charge density calculations. In the study of lattice-reconstruction induced local strain, we averaged the distances between a W atom to its six nearest-neighboring W atoms to give a local lattice constant  $a$  of each monolayer. The local strain is then defined as  $(a - a_0)/a_0$ , where  $a_0$  is the lattice constant of pristine monolayer WSe<sub>2</sub> and WS<sub>2</sub>. In the study of effect from interlayer charge transfer, the stacking orders and interlayer distances were adopted from the long-diagonal of the relaxed moiré lattices. To construct the commensurate bilayer unit cells for DFT calculations, we used the average lattice constant of the relaxed monolayer WSe<sub>2</sub> and WS<sub>2</sub>. All calculations were carried out with Vienna *Ab initio* Simulation Package (VASP) [67, 68], employing an 18×18×1  $k$ -point mesh and an energy convergence criterion of  $1 \times 10^{-6}$  eV. A vacuum spacing of 20 Å was applied along the  $z$  direction to eliminate spurious interactions between periodic images. While van der Waals corrections were essential for structural relaxation, their effects on DFT eigenvalues was negligible and thus omitted in our electronic structure calculations. Additionally, all calculations included spin-orbit coupling effects. We have checked that improving the accuracy of potential field convergence, refining the  $k$ -point mesh, increasing the plane-wave cutoff energy, changing the vdW correction scheme (for example, from DFT-D3 to optB86b-vdW), or changing the exchange-correlation function does not change noticeably the amplitude and spatial profile of the moiré potential.

---

[1] A. K. Geim and I. V. Grigorieva, Van der Waals heterostructures, *Nature* **499**, 419 (2013).

[2] Y. Liu, N. O. Weiss, X. Duan, H.-C. Cheng, Y. Huang, and X. Duan, Van der Waals heterostructures and devices, *Nat. Rev. Mater.* **1**, 16042 (2016).

[3] D. M. Kennes, M. Claassen, L. Xian, A. Georges, A. J. Millis, J. Hone, C. R. Dean, D. N. Basov, A. N. Pasupathy, and A. Rubio, Moiré heterostructures as a condensed-matter quantum simulator, *Nat. Phys.* **17**, 155 (2021).

[4] F. He, Y. Zhou, Z. Ye, S.-H. Cho, J. Jeong, X. Meng, and Y. Wang, Moiré patterns in 2D materials: A Review, *ACS Nano* **15**, 5944 (2021).

[5] Y. Cao, V. Fatemi, S. Fang, K. Watanabe, T. Taniguchi, E. Kaxiras, and P. Jarillo-Herrero, Unconventional superconductivity in magic-angle graphene superlattices, *Nature* **556**, 43 (2018).

[6] Y. Cao, V. Fatemi, A. Demir, S. Fang, S. L. Tomarken, J. Y. Luo, J. D. Sanchez-Yamagishi, K. Watanabe, T. Taniguchi, E. Kaxiras, *et al.*, Correlated insulator behaviour at half-filling in magic-angle graphene superlattices, *Nature* **556**, 80 (2018).

[7] N. P. Wilson, W. Yao, J. Shan, and X. Xu, Excitons and emergent quantum phenomena in stacked 2D semicon-

ductors, *Nature* **599**, 383 (2021).

[8] D. Huang, J. Choi, C. K. Shih, and X. Li, Excitons in semiconductor moiré superlattices, *Nat. Nanotechnol.* **17**, 227 (2022).

[9] K. F. Mak and J. Shan, Semiconductor moiré materials, *Nat. Nanotechnol.* **17**, 686 (2022).

[10] E. C. Regan, D. Wang, E. Y. Paik, Y. Zeng, L. Zhang, J. Zhu, A. H. MacDonald, H. Deng, and F. Wang, Emerging exciton physics in transition metal dichalcogenide heterobilayers, *Nat. Rev. Mater* **7**, 778 (2022).

[11] C. Jin, E. C. Regan, A. Yan, M. I. B. Utama, D. Wang, S. Zhao, Y. Qin, S. Yang, Z. Zheng, S. Shi, *et al.*, Observation of moiré excitons in WSe<sub>2</sub>/WS<sub>2</sub> heterostructure superlattices, *Nature* **567**, 76 (2019).

[12] C. Jin, E. C. Regan, D. Wang, M. I. B. Utama, C.-S. Yang, J. Cain, Y. Qin, Y. Shen, Z. Zheng, K. Watanabe, *et al.*, Identification of spin, valley and moiré quasi-angular momentum of interlayer excitons, *Nat. Phys.* **15**, 1140 (2019).

[13] X. Sun, Y. Zhu, H. Qin, B. Liu, Y. Tang, T. Lü, S. Rahman, T. Yildirim, and Y. Lu, Enhanced interactions of interlayer excitons in free-standing heterobilayers, *Nature* **610**, 478 (2022).

[14] C. Ge, D. Zhang, F. Xiao, H. Zhao, M. He, L. Huang, S. Hou, Q. Tong, A. Pan, and X. Wang, Observation and Modulation of High-Temperature Moiré-Locale Excitons in van der Waals Heterobilayers, *ACS Nano* **17**, 16115 (2023).

[15] L. Huang, C. Ge, B. Xu, Y. Wang, S. Li, X. Luo, H. Zhao, D. Zhang, Z. Zeng, Q. Tong, D. Li, X. Zhu, K. Braun, T. Gao, X. Wang, and A. Pan, Moiré-Orbital-Resolved Excitonic Mott Insulating States and Their Optical and Electric Control in van der Waals Heterostructures, *Phys. Rev. Lett.* **135**, 096902 (2025).

[16] Y. Tang, L. Li, T. Li, Y. Xu, S. Liu, K. Barmak, K. Watanabe, T. Taniguchi, A. H. MacDonald, J. Shan, and K. F. Mak, Simulation of Hubbard model physics in WSe<sub>2</sub>/WS<sub>2</sub> moiré superlattices, *Nature* **579**, 353 (2020).

[17] E. C. Regan, D. Wang, C. Jin, M. I. B. Utama, B. Gao, X. Wei, S. Zhao, W. Zhao, Z. Zhang, K. Yumigeta, *et al.*, Mott and generalized Wigner crystal states in WSe<sub>2</sub>/WS<sub>2</sub> moiré superlattices, *Nature* **579**, 359 (2020).

[18] Y. Shimazaki, I. Schwartz, K. Watanabe, T. Taniguchi, M. Kroner, and A. Imamoglu, Strongly correlated electrons and hybrid excitons in a moiré heterostructure, *Nature* **580**, 472 (2020).

[19] K. P. Nuckolls and A. Yazdani, A microscopic perspective on moiré materials, *Nat. Rev. Mater.* **9**, 460 (2024).

[20] Y. Xu, S. Liu, D. A. Rhodes, K. Watanabe, T. Taniguchi, J. Hone, V. Elser, K. F. Mak, and J. Shan, Correlated insulating states at fractional fillings of moiré superlattices, *Nature* **587**, 214 (2020).

[21] X. Huang, T. Wang, S. Miao, C. Wang, Z. Li, Z. Lian, T. Taniguchi, K. Watanabe, S. Okamoto, D. Xiao, S.-F. Shi, and Y.-T. Cui, Correlated insulating states at fractional fillings of the WS<sub>2</sub>/WSe<sub>2</sub> moiré lattice, *Nat. Phys.* **17**, 715 (2021).

[22] C. Jin, Z. Tao, T. Li, Y. Xu, Y. Tang, J. Zhu, S. Liu, K. Watanabe, T. Taniguchi, J. C. Hone, *et al.*, Stripe phases in WSe<sub>2</sub>/WS<sub>2</sub> moiré superlattices, *Nat. Mater.* **20**, 940 (2021).

[23] E. Liu, T. Taniguchi, K. Watanabe, N. M. Gabor, Y. T. Cui, and C. H. Lui, Excitonic and valley-polarization signatures of fractional correlated electronic phases in a WSe<sub>2</sub>/WS<sub>2</sub> moiré superlattice, *Phys. Rev. Lett.* **127**, 037402 (2021).

[24] S. Miao, T. Wang, X. Huang, D. Chen, Z. Lian, C. Wang, M. Blei, T. Taniguchi, K. Watanabe, S. Tongay, *et al.*, Strong interaction between interlayer excitons and correlated electrons in WSe<sub>2</sub>/WS<sub>2</sub> moiré superlattice, *Nat. Commun.* **12**, 3608 (2021).

[25] D. Chen, Z. Lian, X. Huang, Y. Su, M. Rashetnia, L. Yan, M. Blei, T. Taniguchi, K. Watanabe, S. Tongay, *et al.*, Tuning moiré excitons and correlated electronic states through layer degree of freedom, *Nat. Commun.* **13**, 4810 (2022).

[26] Z. Zhang, E. C. Regan, D. Wang, W. Zhao, S. Wang, M. Sayyad, K. Yumigeta, K. Watanabe, T. Taniguchi, S. Tongay, *et al.*, Correlated interlayer exciton insulator in heterostructures of monolayer WSe<sub>2</sub> and moiré WS<sub>2</sub>/WSe<sub>2</sub>, *Nat. Phys.* **18**, 1214 (2022).

[27] J. Gu, L. Ma, S. Liu, K. Watanabe, T. Taniguchi, J. C. Hone, J. Shan, and K. F. Mak, Dipolar excitonic insulator in a moiré lattice, *Nat. Phys.* **18**, 395 (2022).

[28] X. Wang, X. Zhang, J. Zhu, H. Park, Y. Wang, C. Wang, W. G. Holtzmann, T. Taniguchi, K. Watanabe, J. Yan, *et al.*, Intercell moiré exciton complexes in electron lattices, *Nat. Mater.* **22**, 599 (2023).

[29] G.-B. Liu, D. Xiao, Y. Yao, X. Xu, and W. Yao, Electronic structures and theoretical modelling of two-dimensional group-VIB transition metal dichalcogenides, *Chem. Soc. Rev.* **44**, 2643 (2015).

[30] H. Li, S. Li, M. H. Naik, J. Xie, X. Li, J. Wang, E. Regan, D. Wang, W. Zhao, S. Zhao, *et al.*, Imaging moiré flat bands in three-dimensional reconstructed WSe<sub>2</sub>/WS<sub>2</sub> superlattices, *Nat. Mater.* **20**, 945 (2021).

[31] H. Zhao, S. Yang, C. Ge, D. Zhang, L. Huang, M. Chen, A. Pan, and X. Wang, Tunable Out-of-Plane Reconstructions in Moiré Superlattices of Transition Metal Dichalcogenide Heterobilayers, *ACS Nano* **18**, 27479 (2024).

[32] J. Kang, S. Tongay, J. Zhou, J. Li, and J. Wu, Band offsets and heterostructures of two-dimensional semiconductors, *Appl. Phys. Lett.* **102**, 012111 (2013).

[33] P. Rivera, J. R. Schaibley, A. M. Jones, J. S. Ross, S. Wu, G. Aivazian, P. Klement, K. Seyler, G. Clark, N. J. Ghimire, *et al.*, Observation of long-lived interlayer excitons in monolayer MoSe<sub>2</sub>-WSe<sub>2</sub> heterostructures, *Nat. Commun.* **6**, 6242 (2015).

[34] Y. Jiang, S. Chen, W. Zheng, B. Zheng, and A. Pan, Interlayer exciton formation, relaxation, and transport in TMD van der Waals heterostructures, *Light Sci. Appl.* **10**, 72 (2021).

[35] Q. Tong, H. Yu, Q. Zhu, Y. Wang, X. Xu, and W. Yao, Topological mosaics in moiré superlattices of van der Waals heterobilayers, *Nat. Phys.* **13**, 356 (2017).

[36] F. Wu, T. Lovorn, E. Tutuc, and A. H. MacDonald, Hubbard Model Physics in Transition Metal Dichalcogenide Moiré Bands, *Phys. Rev. Lett.* **121**, 026402 (2018).

[37] H. Yu, G.-B. Liu, J. Tang, X. Xu, and W. Yao, Moiré excitons: From programmable quantum emitter arrays to spin-orbit-coupled artificial lattices, *Sci. Adv.* **3**, e1701696 (2017).

[38] J. Jung, A. Raoux, Z. Qiao, and A. H. MacDonald, Ab initio theory of moiré superlattice bands in layered two-dimensional materials, *Phys. Rev. B* **89**, 205414 (2014).

[39] C. Park, J. Ryou, S. Hong, B. G. Sumpter, G. Kim, and M. Yoon, Electronic properties of bilayer graphene strongly coupled to interlayer stacking and an external

electric field, *Phys. Rev. Lett.* **115**, 015502 (2015).

[40] M. Xia, B. Li, K. Yin, G. Capellini, G. Niu, Y. Gong, W. Zhou, P. M. Ajayan, and Y.-H. Xie, Spectroscopic signatures of AA' and AB stacking of chemical vapor deposited bilayer MoS<sub>2</sub>, *ACS Nano* **9**, 12246 (2015).

[41] H. Yu, Y. Wang, Q. Tong, X. Xu, and W. Yao, Anomalous light cones and valley optical selection rules of interlayer excitons in twisted heterobilayers, *Phys. Rev. Lett.* **115**, 187002 (2015).

[42] C. Zhang, C.-P. Chuu, X. Ren, M.-Y. Li, L.-J. Li, C. Jin, M.-Y. Chou, and C.-K. Shih, Interlayer couplings, Moiré patterns, and 2D electronic superlattices in MoS<sub>2</sub>/WSe<sub>2</sub> hetero-bilayers, *Sci. Adv.* **3**, e1601459 (2017).

[43] N. Sivadas, S. Okamoto, X. Xu, C. J. Fennie, and D. Xiao, Stacking-dependent magnetism in bilayer CrI<sub>3</sub>, *Nano Lett.* **18**, 7658 (2018).

[44] P. H. Jiang, C. Wang, D. Chen, Z. Zhong, Z. Yuan, Z. Y. Lu, and W. Ji, Stacking tunable interlayer magnetism in bilayer CrI<sub>3</sub>, *Phys. Rev. B* **99**, 144401 (2019).

[45] Y. Wang, Z. Wang, W. Yao, G.-B. Liu, and H. Yu, Interlayer coupling in commensurate and incommensurate bilayer structures of transition-metal dichalcogenides, *Phys. Rev. B* **95**, 115429 (2017).

[46] S. Shabani, D. Halbertal, W. Wu, M. Chen, S. Liu, J. Hone, W. Yao, D. N. Basov, X. Zhu, and A. N. Pasupathy, Deep moiré potentials in twisted transition metal dichalcogenide bilayers, *Nat. Phys.* **17**, 720 (2021).

[47] S. Yang, J. Chen, C.-F. Liu, and M. Chen, Evolution of flat bands in MoSe<sub>2</sub>/WSe<sub>2</sub> moiré lattices: A study combining machine learning and band unfolding methods, *Phys. Rev. B* **110**, 235410 (2024).

[48] V. V. Enaldiev, V. Zólyomi, C. Yelgel, S. J. Magorrian, and V. I. Fal'Ko, Stacking domains and dislocation networks in marginally twisted bilayers of transition metal dichalcogenides, *Phys. Rev. Lett.* **124**, 206101 (2020).

[49] V. V. Enaldiev, F. Ferreira, S. J. Magorrian, and V. I. Fal'Ko, Piezoelectric networks and ferroelectric domains in twistronic superlattices in WS<sub>2</sub>/MoS<sub>2</sub> and WSe<sub>2</sub>/MoSe<sub>2</sub> bilayers, *2D Mater.* **8**, 025030 (2021).

[50] S. J. Magorrian, V. V. Enaldiev, V. Zólyomi, F. Ferreira, V. I. Fal'Ko, and D. A. Ruiz-Tijerina, Multifaceted moiré superlattice physics in twisted WSe<sub>2</sub> bilayers, *Phys. Rev. B* **104**, 125440 (2021).

[51] F. Ferreira, S. J. Magorrian, V. V. Enaldiev, D. A. Ruiz-Tijerina, and V. I. Fal'Ko, Band energy landscapes in twisted homobilayers of transition metal dichalcogenides, *Appl. Phys. Lett.* **118**, 241602 (2021).

[52] Q. Tong, M. Chen, F. Xiao, H. Yu, and W. Yao, Interferences of electrostatic moiré potentials and bichromatic superlattices of electrons and excitons in transition metal dichalcogenides, *2D Mater.* **8**, 025007 (2021).

[53] S. Carr, D. Massatt, S. B. Torrisi, P. Cazeaux, M. Luskin, and E. Kaxiras, Relaxation and domain formation in incommensurate two-dimensional heterostructures, *Phys. Rev. B* **98**, 224102 (2018).

[54] Z. Zhu, P. Cazeaux, M. Luskin, and E. Kaxiras, Modeling mechanical relaxation in incommensurate trilayer van der Waals heterostructures, *Phys. Rev. B* **101**, 224107 (2020).

[55] J. Feng, X. Qian, C.-W. Huang, J. Li, Strain-engineered artificial atom as a broad-spectrum solar energy funnel, *Nat. Photon.* **6**, 866 (2012).

[56] K. Li, F. Xiao, W. Guan, Y. Xiao, C. Xu, J. Zhang, C. Lin, D. Li, Q. Tong, S.-Y. Li, *et al.*, Morphology deformation and giant electronic band modulation in long-wavelength WS<sub>2</sub> moiré superlattices, *Nano Lett.* **22**, 5997 (2022).

[57] H. Rostami, F. Guinea, M. Polini, and R. Roldán, Piezoelectricity and valley chern number in inhomogeneous hexagonal 2D crystals, *npj 2D Mater. and Appl.* **2**, 15 (2018).

[58] P. Cudazzo, I. V. Tokatly, and A. Rubio, Dielectric screening in two-dimensional insulators: Implications for excitonic and impurity states in graphane, *Phys. Rev. B* **84**, 085406 (2011).

[59] L. Li and M. Wu, Binary compound bilayer and multilayer with vertical polarizations: two-dimensional ferroelectrics, multiferroics, and nanogenerators, *ACS Nano* **11**, 6382 (2017).

[60] S. Plimpton, Computational limits of classical molecular dynamics simulations, *Comput. Mater. Sci.* **4**, 361 (1995).

[61] F. H. Stillinger and T. A. Weber, Computer simulation of local order in condensed phases of silicon, *Phys. Rev. B* **31**, 5262 (1985).

[62] J.-W. Jiang and Y.-P. Zhou, Handbook of Stilinger-Weber Potential Parameters for Two-Dimensional Atomistic Crystals, edited by J.-W. Jiang and Y.-P. Zhou (IntechOpen, Rijeka, 2017).

[63] M. H. Naik, I. Maity, P. K. Maiti, and M. Jain, Kolmogorov-Crespi potential for multilayer transition-metal dichalcogenides: capturing structural transformations in moiré superlattices, *J. Phys. Chem. C* **123**, 9770 (2019).

[64] A. N. Kolmogorov and V. H. Crespi, Registry-dependent interlayer potential for graphitic systems, *Phys. Rev. B* **71**, 235415 (2005).

[65] W. Kohn and L. J. Sham, Self-consistent equations including exchange and correlation effects, *Phys. Rev.* **140**, A1133 (1965).

[66] J. M. Soler, E. Artacho, J. D. Gale, A. García, J. Junquera, P. Ordejón, and D. Sánchez-Portal, The SIESTA method for ab initio order-N materials simulation, *J. Phys.: Condens. Matter* **14**, 2745 (2002).

[67] G. Kresse and J. Hafner, Ab initio molecular dynamics for liquid metals, *Phys. Rev. B* **47**, 558 (1993).

[68] G. Kresse and J. Furthmüller, Efficient iterative schemes for ab initio total-energy calculations using a plane-wave basis set, *Phys. Rev. B* **54**, 11169 (1996).